Materials Horizons

ROYAL SOCIETY OF CHEMISTRY

COMMUNICATION

View Article Online
View Journal | View Issue

Check for updates

Cite this: *Mater. Horiz.*, 2024, **11**, 3375

Received 14th March 2024,
Accepted 23rd April 2024

DOI: 10.1039/d4mh00286e

rsc.li/materials-horizons

Heterogeneous CNF/MoO_3 nanofluidic membranes with tunable surface plasmon resonances for solar-osmotic energy conversion†

Mengmeng Zheng,‡[a] Pei Liu,‡*[ab] Pengfei Yan,[a] Teng Zhou,[d] Xiangbin Lin,[c] Xin Li,[c] Liping Wen *[c] and Qun Xu *[ab]

Two-dimensional (2D) nanofluidic membranes are competitive candidates for osmotic energy harvesting and have been greatly developed. However, the use of diverse inherent characteristics of 2D nanosheets, such as electronic or optoelectronic properties, to achieve intelligent ion transport, still lacks sufficient exploration. Here, a cellulose nanofiber/molybdenum oxide (CNF/MoO_3) heterogeneous nanofluidic membrane with high performance solar-osmotic energy conversion is reported, and how surface plasmon resonances (SPR) regulate selective cation transport is revealed. The SPR of amorphous MoO_3 endows the heterogeneous nanofluidic membranes with tunable surface charge and good photothermal conversion. Through DFT calculations and finite element modeling, the regulation of electronic and optoelectronic properties on the surface of materials by SPR and the influence of surface charge density and temperature gradient on ion transport in nanofluidic membranes are demonstrated. By mixing 0.01/0.5 M NaCl solutions using SPR and photothermal effects, the power density can achieve a remarkable value of $\approx$13.24 W m^{-2}, outperforming state-of-the-art 2D-based nanofluidic membranes. This work first reveals the regulation and mechanism of SPR on ion transport in nanofluidic membranes and systematically studies photon–electron–ion interactions in nanofluidic membranes, which could also provide a new viewpoint for promoting osmotic energy conversion.

New concepts

The energy crisis has become a critical issue for human society due to the ever-increasing energy demand. 2D nanofluidic membranes as competitive candidates have received widespread attention. However, further basic research and the use of diverse inherent characteristics of 2D nanosheets, such as electronic or optoelectronic properties, to achieve intelligent ion transport, still lack sufficient exploration. Our work first reveals the regulation and mechanism of SPR on ion transport in nanofluidic membranes and explores the potential of solar-osmotic energy conversion based on CNF/MoO_3 heterogeneous nanofluidic membranes. Experimental details and theoretical calculations indicate that the higher surface charge and temperature of the nanofluidic membranes tuned by SPR and photothermal effects help to improve ion selectivity and accelerate cation diffusion, achieving high-performance solar-osmotic energy conversion. This work demonstrates a systematic study of photon–electron–ion interactions in nanofluidic membranes and provides an ideal viewpoint for promoting osmotic energy conversion.

Introduction

Access to sustainable, abundant, and inexpensive energy sources has been extensively explored because of the continuous exploitation and consumption of fossil energy.[1,2] In nature, water and solar are not only vital to life but also represent the largest carriers of energy on earth.[3,4] Osmotic energy, stored as an ionic gradient between seawater and fresh water, has been identified as a promising source of renewable energy and attracted significant attention.[5,6] Nanofluidic membranes with tailored ion transport dynamics has been promoted as a novel candidate to efficiently harvest renewable osmotic energy and relevant research has emerged in the past few decades.[7–9] In particular, nanofluidic membranes constructed from 2D materials have led to advances in their application in osmotic energy due to their high surface charge, precisely controlled layer spacing, and excellent processability.[10,11] Although 2D nanofluidic membranes have received wide attention, further basic research and the use of diverse inherent characteristics of 2D nanosheets,

---

[a] *Henan Institute of Advanced Technology, Zhengzhou University, Zhengzhou 450052, P. R. China. E-mail: peiliu@zzu.edu.cn, qunxu@zzu.edu.cn*

[b] *College of Materials Science and Engineering, Zhengzhou University, Zhengzhou 450052, P. R. China*

[c] *CAS Key Laboratory of Bio-inspired Materials and Interfacial Science, Technical Institute of Physics and Chemistry, Chinese Academy of Sciences, Beijing 100190, P. R. China. E-mail: wen@mail.ipc.ac.cn*

[d] *College of Mechanical and Electrical Engineering, Hainan University, Haikou, 570228, Hainan, P. R. China*

† Electronic supplementary information (ESI) available. See DOI: https://doi.org/10.1039/d4mh00286e

‡ These authors contributed equally to this work.

such as electronic or optoelectronic properties, to achieve intelligent ion transport still lack adequate exploration. Besides, the conversion of osmotic energy coupled with other energy sources has also attracted widespread attention.[12,13] Solar energy as one of the most abundant energy sources on earth has been extensively developed based on photoelectronic and photothermal effects and realized the potential application in nanofluidic devices and miniature osmotic energy conversion systems.[14–16] Based on the photoelectric effect, the light-induced separation of electrons and holes in the membrane resulted in a transmembrane potential difference, which could be utilized for the construction of artificial light-driven ion pumps, ionic photoelectric conversion, and enhanced osmotic energy generation.[17–19] Furthermore, the introduction of the photothermal effect can directly lead to the generation of a localized heat or temperature gradient, resulting in ion active transport and thermally enhanced osmotic energy harvesting.[20–22] With the discovery of a series of novel light regulated ion transport behaviors in nanofluidic membranes, improving the basic understanding of ion transport mechanisms remains an extremely challenging task. Therefore, both the construction of nanostructures with inherent electronic/optoelectronic properties and the development of novel photo-regulated ion transport mechanisms are urgently needed, especially for practical applications such as solar-osmotic energy conversion systems.

As a new kind of materials, 2D amorphous materials not only exhibit unique structural merits of short-range structural ordering and isotropic amorphous characteristics, but also are endowed with exposed atoms and the confinement of electrons.[23,24] SC-CO_2 has shown great potential in the fabrication of 2D amorphous materials, which can exhibit both vapor- and liquid-like behaviors, including near-zero surface tension, low viscosity, high diffusion coefficients, excellent wetting of surfaces, and strong solvating power.[25–27] 2D amorphous MoO_3 nanosheets with tunable SPR could be obtained using SC-CO_2.[28] Their electronic properties can be tuned to make them suitable for developing a variety of future electronic and optical devices. SPR, which is the strong interaction between light and nanomaterials, could result in elevated electromagnetic fields and a higher free electron concentration.[29–31] However, how the SPR changes the surface properties of nanofluidic membranes to regulate ion transport for osmotic energy conversion is still unknown, but might open a new avenue for synergetic energy harvesting.

Herein, we demonstrated an efficient solar-osmotic energy conversion system assisted by SPR and photothermal effects based on heterogeneous CNF/MoO_3 nanofluidic membranes (Fig. 1). By mixing artificial river water (0.01 M NaCl) and seawater (0.5 M NaCl), the maximum power density of this composite system could achieve a value of approximately 7.86 W m^{-2}. Upon light illumination, hydrogen-doped amorphous MoO_3 nanosheets exhibit tunable SPR and lead to a higher free electron concentration, which can increase the surface charge of the nanofluidic membranes to promote cation transmembrane transport. Using SPR, the output power

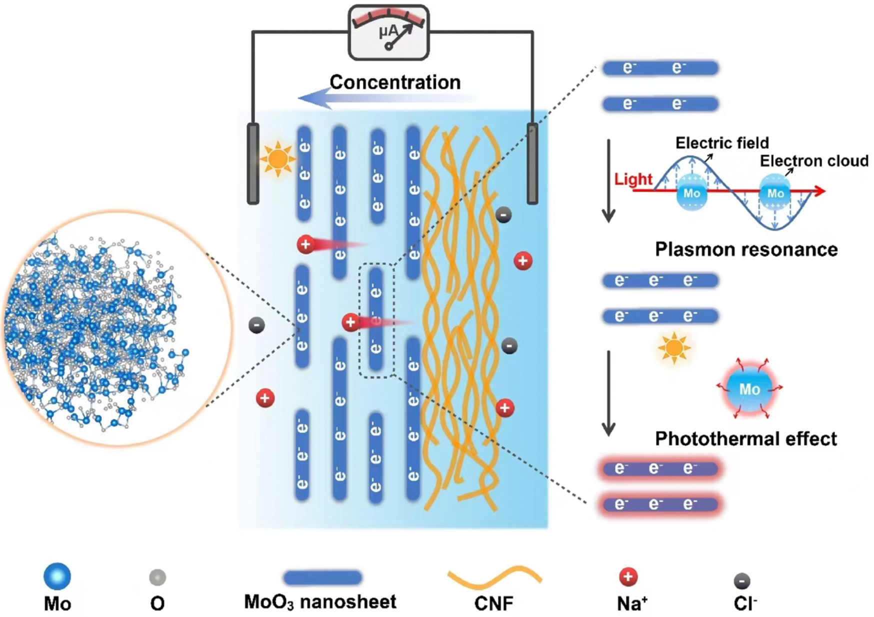

Fig. 1 Schematic representation of the heterogeneous CNF/MoO_3 nanofluidic membranes with tunable surface plasmon resonances for solar-osmotic energy conversion. The heterogeneous nanofluidic membranes were fabricated by a two-step vacuum-assisted filtration with MoO_3 nanosheets and cellulose nanofibers (CNF). The Na^+ can be driven to pass through the nanofluidic membranes by a chemical potential gradient, and a cation current is formed. More importantly, active tuning of the surface plasmon resonances in 2D MoO_3 could be simply realized by irradiating the suspension of 2D nanosheets with solar energy, which results in higher surface free electron concentrations and better photothermal conversion. The higher surface charge tuned by the surface plasmon resonances improves the selectivity and gradient-driven transmembrane ion diffusion. Additionally, owing to the better photothermal conversion, light-induced heat could facilitate ion migration. The tunable surface plasmon resonances and photothermal conversion synergistically endow the system with enhanced ion selectivity and flux, enabling high-performance energy conversion.

density could be enhanced to about 9.07 W m^{-2}. Additionally, benefitting from the photothermal effects, the power density was further improved to 13.24 W m^{-2}. The achievable high power output performance could be ascribed to the higher surface charge and temperature of the nanofluidic membranes tuned by the SPR and photothermal effect of MoO_3. Both experiments and theoretical calculations help us to understand the mechanism of how SPR and temperature gradients dominate the selective ion transport process. Our work demonstrates the regulation of diverse inherent characteristics of 2D nanosheets to achieve intelligent ion transport, showing their promise for solar-osmotic energy conversion.

Results and discussion

Amorphous two-dimensional MoO_3

Amorphous MoO_3 was obtained using SC-CO_2 (Fig. 2a and Note S1, ESI†).[28] The oxygen incorporation in MoS_2 was achieved during the annealing process, in which oxygen atoms can replace sulfur atoms, and the regular atomic arrangement is destroyed. The adsorption strength of small molecules on the amorphous surface is stronger than that on the crystal surface. Compared to organic solvents, SC-CO_2 has a smaller molecular size, and when it reaches the supercritical state, it has the properties of both vapor and liquid, which makes it easy to penetrate into the lamellar material and generate expansion or swelling to achieve intercalation, modification, and exfoliation. Thanks to the low surface tension, low viscosity, and high diffusion features, CO_2 molecules can easily enter the intermediate layer of MoO_3 and the adsorption of CO_2 molecules can lead to stabilization of amorphous MoO_3. In addition, the stronger interaction between CO_2 and amorphous MoO_3 may allow diffusive atomic disordering to achieve strain engineering.[32–34] The morphology of the samples was characterized by transmission electron microscopy (TEM) as shown in Fig. 2b. Both ultrasonicated and SC-CO_2 treated samples showed sheet-like morphology as can be seen from the low-magnification TEM images. To further

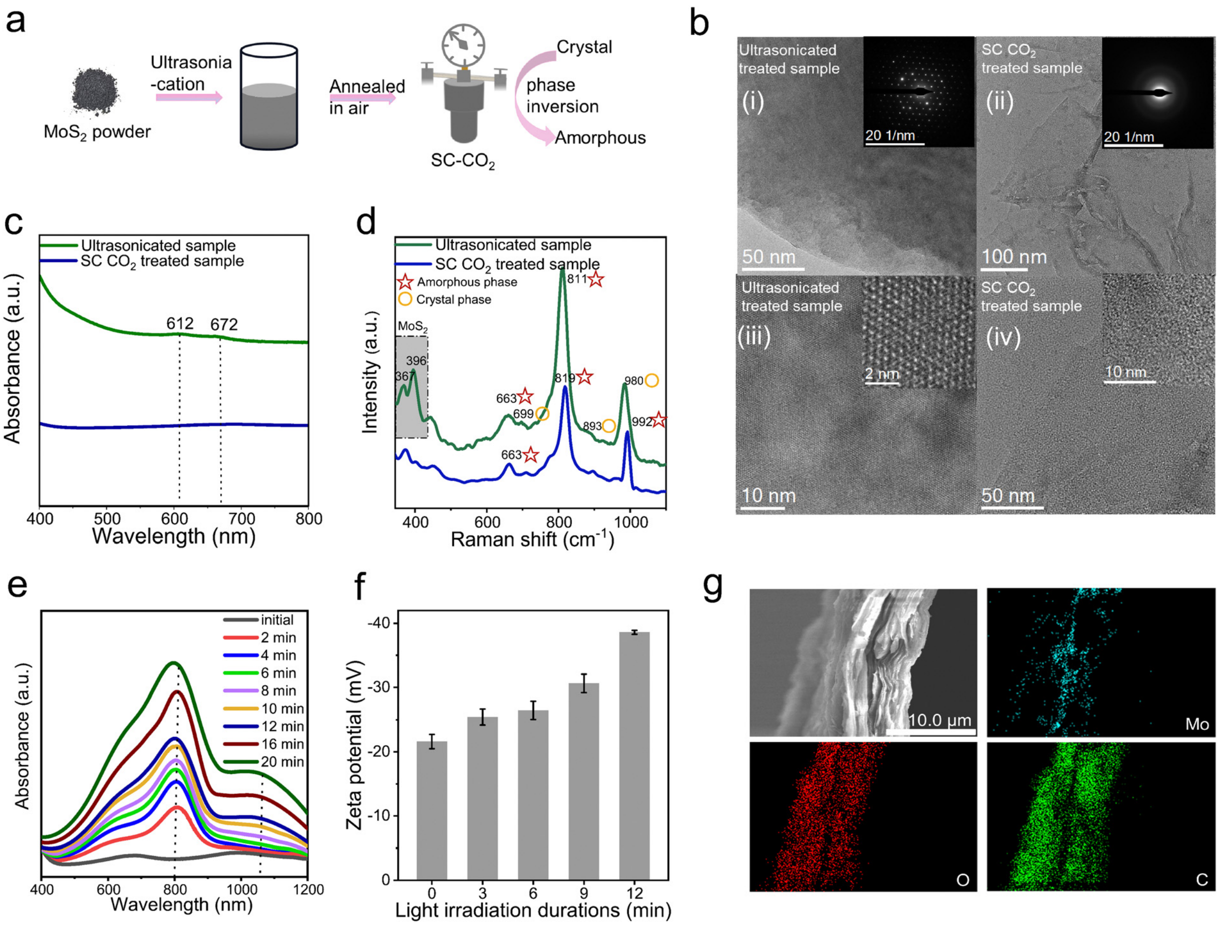

Fig. 2 Characterizations of CNF/MoO_3 membranes. (a) Schematic illustration of the amorphous MoO_3 nanosheets prepared using SC-CO_2. (b) HRTEM image and the corresponding SAED pattern of the ultrasonicated and SC-CO_2 treated samples. (c) UV/Vis-NIR absorption spectra of supernatant solutions. Inset: Photograph of left: ultrasonicated MoO_3 nanosheets and right: SC-CO_2 treated MoO_3 nanosheets. (d) Raman spectra. (e) UV/Vis-NIR absorbance spectra of the SC-CO_2 treated MoO_3 suspensions before and after irradiation at different xenon lamp irradiation durations with a power of 1.3 W cm^{-2}. (f) Zeta potential of MoO_3 nanosheets at different solar light irradiation durations. When increasing the irradiation duration, the zeta potential of the $MoO_{3(SC)}$ nanosheets becomes more negative. (g) Elemental mapping analyses of the CNF/$MoO_{3(SC)}$ membrane.

verify the crystal structure of the prepared samples, the lattice arrangement could be clearly seen in the high-resolution TEM (HRTEM) images. Fig. 2b-iii shows the obvious lattice structure of the 2D MoO_3 nanosheets after sonication, while the HRTEM image of the SC-CO_2 treated sample indicated strong disordered atomic arrangement and even the short-range sequence of the nanostructure could not be clearly observed (Fig. 2b-iv). The corresponding selected area electron diffraction (SAED) pattern (Fig. 2b-i inset) of the ultrasonicated sample clearly distinguishes diffraction spots, suggesting the existence of small nanodomains with short-range ordering. However, after SC-CO_2 treatment, some of the lattice fringes appear disordered because of the CO_2 intercalation. This disorder is confirmed by the SAED pattern of the polycrystalline ring (Fig. 2b-ii inset), demonstrating the amorphous properties of the prepared samples. The optical properties of ultrasonicated and SC-CO_2 treated samples were investigated by UV/Vis-NIR absorbance spectroscopy (Fig. 2c). The absorption peaks at 612 and 672 nm of the ultrasonicated nanosheets are related to the direct excitonic transitions of MoS_2 nanosheets at the *K*-point in the Brillouin zone,[35] while no absorption peak could be found for the SC-CO_2 treated nanosheets. Additionally, Raman spectra acquired for the two samples confirmed the phase inversion of MoO_3 under SC-CO_2 treatment (Fig. 2d). Compared with the sample under SC-CO_2 treatment, the ultrasonicated sample showed more characteristic peaks, including unoxidized MoS_2 peaks at 367 cm^{-1} and 396 cm^{-1}, crystalline phase h-MoO_3 peaks at 699 cm^{-1}, 893 cm^{-1} and 980 cm^{-1} and amorphous phase α-MoO_3 peaks at 663 cm^{-1} and 811 cm^{-1}. However, there were only α-MoO_3 characteristic peaks at 663 cm^{-1}, 819 cm^{-1} and 992 cm^{-1} in the SC-CO_2 treated sample. It can be concluded that metastable h-MoO_3 can be converted to stable amorphous α-MoO_3 under SC-CO_2 treatment. From the XRD patterns (Fig. S2, ESI†), the SC-CO_2 treated sample showed only a weak line shape in the range of 20 to 30°, indicating the poor crystallinity. Meanwhile, for the ultrasonicated sample, it was worthy noting that the diffraction peaks at 19.4° and 25.8° correspond to the (200) plane of h-MoO_3 and the (040) plane of α-MoO_3, respectively, suggesting a crystal structure. X-ray photoelectron spectroscopy (XPS) was further performed to assess the surface chemical composition and chemical state of the as-prepared MoO_3 nanosheets (Fig. S3, ESI†). Under the irradiation of a xenon lamp with a power of 1.3 W cm^{-2}, the color of the solution continuously deepened with a longer illumination time (Fig. S4, ESI†), and the corresponding UV/Vis-NIR absorption spectrum in Fig. 2e shows dual optical absorption bands centered at 806 and 1059 nm, respectively. These absorption bands gradually increased and underwent a slight red shift from 806 to 812 nm and from 1059 to 1065 nm, indicating that the SPR effect was enhanced with a longer irradiation time. In contrast, the absorption peak of the CNF solution did not change as the light irradiation time increased (Fig. S5, ESI†).

Characterization of heterogeneous nanofluidic membranes

The heterogeneous nanofluidic membranes were fabricated *via* a two-step vacuum-assisted filtration with SC-CO_2 treated MoO_3 nanosheets ($MoO_{3(SC)}$) and cellulose nanofibers (CNF) (Fig. S1 and Note S2, ESI†). The as-prepared nanofluidic membranes are free-standing and transparent (Fig. S6, ESI†). The XPS spectrum provided the compositional evidence of heterogeneous nanofluidic membranes with the high peak intensity of O 1s at 531.9 eV, C 1s at 284.9 eV, and Mo 3d at 233.9 eV (Fig. S7, ESI†). The zeta potential of amorphous MoO_3 nanosheets at different solar light irradiation durations is shown in Fig. 2f. Longer irradiation durations increased the degree of H^+ intercalation and caused higher substoichiometric levels (Note S3, ESI†),[29,36] resulting in higher free electron concentrations and increasing the zeta potential from −21.6 mV to −38.6 mV within 0 to 12 min of the light irradiation. The prepared CNF/$MoO_{3(sc)}$ membranes were analyzed using scanning electron microscopy (SEM). The SEM characterization of the cross section exhibited a heterogeneous nanofluidic membrane with a ~8 μm thickness. Elemental mapping analyses of the CNF/$MoO_{3(SC)}$ membrane demonstrated that the elements C and O were distributed in the entire membrane, whereas Mo was distributed only on one side of the heterogeneous nanofluidic membrane (Fig. 2g and Fig. S8, ESI†).

Ion transport and high-performance osmotic energy conversion

The transmembrane ionic transport properties of the nanofluidic membranes were investigated using a symmetrical two-compartment electrochemical cell. The ionic current increases linearly with the applied voltage and the CNF/$MoO_{3(SC\text{-}L12)}$ membrane shows the highest ionic current (Fig. 3a). The ion conductivity curve of all membranes deviates from the linear bulk behavior and gradually stabilizes when the concentrations are below 0.1 M (Fig. 3b). The deviation from the bulk behavior (dashed line) at low concentrations (≤0.1 M) indicates that the ionic transport across the membrane is controlled by the surface charge.[37–39] It is worth noting that, compared with other membranes, CNF/$MoO_{3(SC\text{-}L12)}$ shows the highest transmembrane conductance. The conductance G for all salt concentrations can be calculated as follows:[40,41]

$$G = (\mu_{K^+} + \mu_{Cl^-})cN_A e\frac{wh}{\mathrm{d}} + 2\mu_{K^+}\sigma_s\frac{w}{d} \tag{1}$$

where μ_i is the mobility, c_i is the ion concentration, N_A is the Avogadro constant, e is the electron charge, σ_s is the effective surface charge density, and h, w, and d are the height, the width, and the length of the channels, respectively. The excellent ion transport and cation selectivity of the composite membrane paved the way for osmotic energy conversion. Here, we use a homemade device to determine the ability of the nanofluidic membranes in harvesting osmotic energy (Fig. S9, ESI†). The membranes were placed in an asymmetric electrolyte (NaCl, C_L = 0.01 M; C_H = 0.5 M). Driven by a chemical potential gradient, cations preferentially transport through the negatively charged nanofluidic membranes from the high-concentration side to the low-concentration side, generating the open-circuit voltage (V_{oc}) and short-circuit current (I_{sc}), which can be obtained from the intercepts of voltage and current axes. The ion current is recorded under a concentration gradient from the $MoO_{3(SC)}$ side fixed at 0.01 M concentration to the CNF side

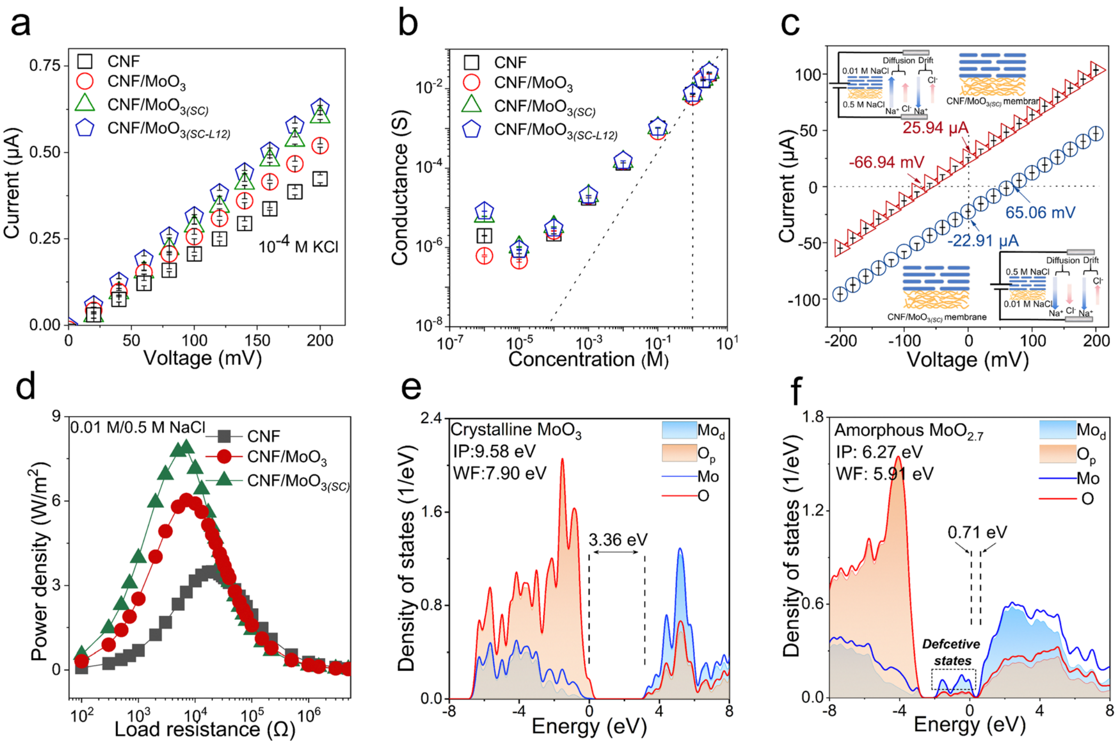

Fig. 3 Ion transport and high-performance osmotic energy conversion. (a) I–V curves of four nanofluidic membranes in a neutral KCl electrolyte with a concentration of 10^{-4} M. (b) Measurement of the transmembrane ionic conductance of four membranes in KCl electrolyte. The ion conductance deviates from the volume value (dashed line) when the KCl concentration is less than 0.1 M, indicating that the transmembrane ion transport is controlled by the surface charge. The CNF/$MoO_{3(SC\text{-}L12)}$ membrane showed the highest ion conductance at low concentrations. (c) I–V curves of the CNF/$MoO_{3(SC)}$ at a 50-fold gradient under two configurations of forward and reverse diffusion directions. (d) Recorded output power density of three membranes as a function of the load resistances (R_L) under a 50-fold concentration gradient. The corresponding maximum output power density of 3.49 W m^{-2} (CNF), 6.04 W m^{-2} (CNF/MoO_3), and 7.86 W m^{-2} (CNF/$MoO_{3(SC)}$) can be realized. (e) Calculated density of states (DOS) of crystal MoO_3. (f) Calculated DOS of amorphous $MoO_{2.7}$.

fixed at 0.5 M concentration (red curve in Fig. 3c) and under a reversed salinity gradient (blue curve in Fig. 3c). The former has a larger I_{sc} of 25.94 μA and is considered as an advantageous direction in the following tests. To further evaluate the osmotic energy conversion capability, the setup was connected to an external electronic load resistor (R_L) to output the harvested electric power. The current density driven by the chemical potential gradient decreased with the increase of the external load (Fig. S10, ESI†). The output power density ($P = I^2 \times R_L/S$) reached its peak when the external resistance was approximately equal to the internal resistance of the membrane. The tested membrane area (S) was about 3 × 10^4 μm^2. For CNF/$MoO_{3(SC)}$ membranes, the maximum power density could reach 7.86 W m^{-2} for the 50-fold concentration gradient, which was higher than that of the pure CNF (3.49 W m^{-2}) and CNF/MoO_3 (6.04 W m^{-2}) membranes (Fig. 3d). Current density and power density under the other two concentration gradients were also tested (Fig. S11–13, ESI†). The CNF/$MoO_{3(SC)}$ membranes showed the highest output power density among these nanofluidic membranes at all concentration gradients, which benefits from the higher surface charge density of $MoO_{3(SC)}$ described earlier. To further elucidate the physical mechanisms of amorphous MoO_3 assisting in enhancing ion transport and osmotic energy conversion, density functional theory (DFT) simulations were conducted (Note S5, ESI†).[42] Owing to quantum confinement effects, the bandgap of the simulated monolayer crystalline MoO_3 is 3.36 eV, marginally larger than that of bulk MoO_3. Time dependent density functional theory (TD-DFT) simulations of its electronic excitations revealed that the valence band electrons of crystalline MoO_3 cannot be excited by visible light, thereby resulting in its lack of visible light absorption activity (Fig. S14, ESI†). Concurrently, the electron ionization potential (IP) and work function (WF) of crystalline MoO_3 are as high as 9.58 eV and 7.9 eV, respectively, meaning it is difficult for crystalline MoO_3 to become an electron donor (Fig. 3e). Defect-free amorphous MoO_3 had been constructed using the simulated melt-quench scheme to confirm the effect of amorphous phase transition.[43–45] The study of electronic state density revealed that the amorphous phase transition results in a slight decrease in the bandgap width from 3.36 eV to 3.33 eV, accompanied by the formation of strong localized states at the bottom of the conduction band. This implied that a mere transition to the amorphous phase does not enhance the absorption activity of MoO_3 for visible and near-infrared light, but rather augment its intrinsic absorption activity in the ultraviolet region. Indeed, SC-CO_2 treatment successfully introduced a large number of defects and dominated the formation of amorphous MoO_{3-x}.

Therefore, the amorphous $MoO_{2.7}$ generated through simulations was further studied. Electronic studies indicated that the presence of oxygen defects in amorphous $MoO_{2.7}$ led to the emergence of numerous defect states within the original bandgap, thereby significantly reducing its bandgap to 0.71 eV. Further simulations of electronic excitations revealed that this evolution in the electronic structure substantially enhanced the light absorption activity of amorphous $MoO_{2.7}$ in the visible and near-infrared regions. Importantly, the Fermi level of amorphous $MoO_{2.7}$ exhibited a significant shift to the right compared to crystalline MoO_3, indicating a higher internal electron concentration.[46–48] Simultaneously, the IP and WF of amorphous $MoO_{2.7}$ decreased to 6.27 eV and 5.91 eV, respectively, signifying a marked enhancement in its electron departure capability (Fig. 3f). In summary, the DFT calculations revealed that the SC-CO_2-driven amorphous defect engineering of MoO_3 significantly augments its electron concentration and electron delocalization, as well as its light absorption activity in the visible and near-infrared regions (Fig. S15, ESI†). This unveils the electronic mechanism of SPR of amorphous MoO_3, as well as its enhanced ion transport and osmotic energy conversion capabilities.

Surface plasmon resonances promoted osmotic energy conversion

SPRs are the collective oscillations of surface free electrons confined to the nanoscale by light-induced excitations, which enables extremely large electric field enhancements around the nanomaterials (Fig. 4a).[49,50] The SPRs of amorphous $MoO_{3(SC)}$ nanosheets have been tested. Upon light excitation of the amorphous $MoO_{3(SC)}$ nanosheets, tunable SPRs in the visible and near-IR regions were achieved by light-driven H^+ intercalation (Note S3, ESI†). When the MoO_3 nanosheets were irradiated with light, excitons and holes were generated (Note S3, eqn (1), ESI†). Then, the protons can be obtained from the reaction of the adsorbed water with the holes (Note S3, eqn (2), ESI†). The resulting protons can diffuse into the tunnels and cavities of the MoO_3 lattice, while the oxygen radicals may combine with each other to produce O_2 gas and escape. The photogenerated excitons react with MoO_3 and protons (Note S3, eqn (3), ESI†).[29,36]

As a result, there were more free electrons on the surface of MoO_3, which promoted transmembrane cation transport and further improved osmotic energy conversion performance. To further explore the influence of SPRs on ion transport and osmotic energy conversion, the current density and power density of CNF/$MoO_{3(SC)}$ and CNF/$MoO_{3(SC\text{-}L12)}$ membranes were compared (Fig. 4b and c). The current density driven by the chemical potential gradient decreases as the external load (R_L) increases, and the output power density reaches its peak (P_{max}) with an intermediate load resistance. The power density of the CNF/$MoO_{3(SC\text{-}L12)}$ membrane could reach ~9.07 W m^{-2}, which is significantly higher than that of the CNF/$MoO_{3(SC)}$ system, which was 7.86 W m^{-2}. The higher surface charge

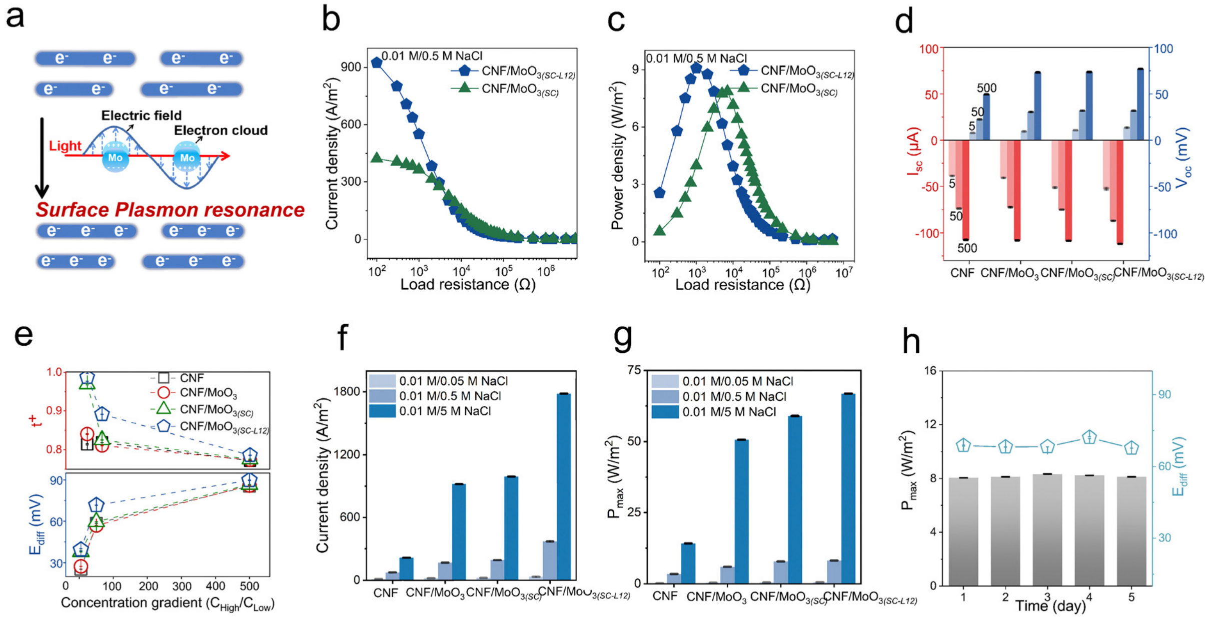

Fig. 4 Surface plasmon resonances promoted osmotic energy conversion. (a) Schematic representation of surface plasmon resonance enhanced surface free electron concentration. (b) and (c) Osmotic energy conversion behaviors of the CNF/$MoO_{3(SC)}$ and CNF/$MoO_{3(SC\text{-}L12)}$ composite membranes. (d) Comparison of the V_{oc} and I_{sc} of the four kinds of nanofluidic membranes under different concentration gradients. (e) Calibrated diffusion potential (E_{diff}) and transmembrane ion transference number (t_+) of the membranes under a series of NaCl salinity gradients. The low concentration side is set to 0.01 M. (f) and (g) The maximum output power density and the corresponding current density of the four nanofluidic membranes under 5-fold, 50-fold, and 500-fold concentration gradients, respectively. Both the maximum power density and the corresponding current density increased with the increase of the concentration gradients, and the CNF/$MoO_{3(SC\text{-}L12)}$ membrane had the largest power density and current density. (h) The working stability of the CNF/$MoO_{3(SC\text{-}12)}$ composite membrane-based energy conversion device.

benefiting from the SPRs is favorable for the high-performance energy conversion process. Defect-free amorphous MoO_3 had been constructed using DFT simulations to confirm the effect of the SPR-dominated increase in the concentration of oxygen defects. Electronic studies revealed that the amorphous phase transition results in a slight decrease in the bandgap width of MoO_3 from 3.36 eV in the crystalline phase to 3.33 eV in the amorphous phase, accompanied by the formation of a strong localized state at the bottom of the conduction band. These findings starkly contrast with the electronic and spectroscopic simulation outcomes for the abovementioned amorphous $MoO_{2.7}$, further elucidating the mechanism by which SPR amplifies the concentration of oxygen defects to improve ion transport and osmotic energy conversion (Fig. S16, ESI†). To further evaluate the energy conversion capability of the membranes, we further tested the power generation by collecting I–V curves under a series of concentration gradients. The corresponding I_{sc} and V_{oc} values increase gradually (Fig. 4d). Obviously, the CNF/$MoO_{3(SC\text{-}L12)}$ membrane has the highest V_{oc} and I_{sc} under different concentration gradients. Moreover, the diffusion potential (E_{diff}) could be calculated by the electrode calibration process (Fig. S17, Note S4 and Table S1, ESI†) that deducts the contribution of redox potential (E_{redox}) due to the unequal electrode reaction in different solutions. E_{diff} can be described as follows:

$$E_{diff} = V_{oc} - E_{redox} \tag{2}$$

It is worth noting that the ion selectivity of nanofluidic membranes is the origin of E_{diff}. The cation transference number (t_+) can be calculated from E_{diff} and it equals 1 for ideal selectivity and 0.5 for nonselective membranes:[51–53]

$$t_+ = \frac{1}{2} \times \left[\frac{E_{diff}}{\frac{RT}{ZF} \ln\left(\frac{a_{high}}{a_{low}}\right)} + 1 \right] \tag{3}$$

Here, R, T, F and Z refer to the gas constant, temperature, Faraday constant, and charge number, respectively. a_{high} and a_{low} are the activities of NaCl on the high concentration and low concentration sides, respectively. Overall, we have listed the E_{diff} and the calculated transmembrane t_+ values of the four membranes in Fig. 4e. Compared with others, the CNF/$MoO_{3(SC\text{-}L12)}$ membrane has the highest E_{diff} and t_+ regardless of the concentration gradients, which could be ascribed to the SPRs of MoO_3, which can create more surface free electrons and eventually promote the ion selectivity and transport. Moreover, the CNF/$MoO_{3(SC\text{-}L12)}$ membranes exhibited ultrahigh charge selectivity, as indicated by their t_+, reaching up to 0.98. As the membrane is cation-selective, the better the ion selectivity, the more remarkable the charge separation that will occur, resulting in a higher power output (Fig. 4f and g). Additionally, the maximum output power density and E_{diff} show no obvious attenuation even after 1 week, indicating the excellent long-term stability of these composite nanofluidic membranes and their promising application potential in osmotic energy conversion (Fig. 4h).

Photo-enhanced osmotic energy conversion system

Light was introduced into our system as an ideal external physical field due to its remote maneuverability and sustainability. However, considering the poor light stability of Ag/AgCl electrodes, a light-proof shield was used to prevent the Ag/AgCl electrodes from being exposed to light. When light irradiation is applied on the low concentration side (MoO_3 side), the temperature of the irradiation area increases due to the good photothermal effect of MoO_3, and a temperature difference is formed. Thus, the photothermal-induced temperature gradient could be used to drive ion transport across the nanofluidic membranes, achieving photo-enhanced ion transport and osmotic energy conversion (Fig. 5a). Under asymmetric light irradiation, the output power density of the CNF/$MoO_{3(SC\text{-}L12)}$ membrane increased from 8.19 to 13.24 W m^{-2}, achieving an increase of approximately 61.5%. Benefiting from the higher surface charge concentration and excellent photothermal effect, the output power density of CNF/$MoO_{3(SC\text{-}L12)}$ increases by a larger amount after illumination compared to the other membranes (Fig. 5b). The photo-enhanced osmotic energy conversion performance of CNF/$MoO_{3(SC\text{-}L12)}$ membranes was also higher than that of the other membranes (Fig. 5c and Fig. S18, ESI†), which could be ascribed to the higher light absorption and the better photothermal conversion behaviors (Fig. S19 and 20, ESI†). Moreover, the magnitude of the light-enhanced power density increases with light intensity (Fig. 5d and Fig. S21, ESI†). The observed photo-enhancement phenomenon can be attributed to the photothermal effect and cation–exciton interaction. Due to the photothermal effect of MoO_3, light irradiation onto the MoO_3 side could significantly increase the temperature, which could amplify the thermophoretic mobility of ions, thereby decreasing the ion transport resistance and eliminating ion concentration polarization (ICP) to some extent.[54,55]

Simultaneously, the contribution of the photogenerated excitons was unveiled through the analysis of natural transition orbitals (NTOs) based on TD-DFT calculations. Electronic structure investigations indicated that the adsorption of Na^+ can form localized Na empty orbitals at the bottom of the conduction band in amorphous $MoO_{2.7}$. This implied that the electrons in the defect states can transfer to these empty orbitals (Fig. 5e). Concurrently, the spatial analysis of excited state electrons confirmed that the photoexcited state electrons in amorphous $MoO_{2.7}$ can localize around Na^+, and the exciton–hole coupling can further enhance the adsorption of Na^+ on the surface of the amorphous MoO_3 material (Fig. 5f and Fig. S22, ESI†). Thus, light irradiation increases the adsorption of Na^+ on the amorphous $MoO_{2.7}$ surface for improved selectivity, which promotes ion transport and eventually the osmotic energy conversion. The synergy of the cation–exciton interaction and photothermal effects enhances cation selectivity and ion transport in the nanofluidic membranes. It should be noted that our work realized high-performance osmotic energy conversion among the membrane-based nanofluidic membranes in the same testing area (Fig. S23, ESI†). Finite-element simulations based on the Poisson–Nernst–Planck (PNP) theory are also

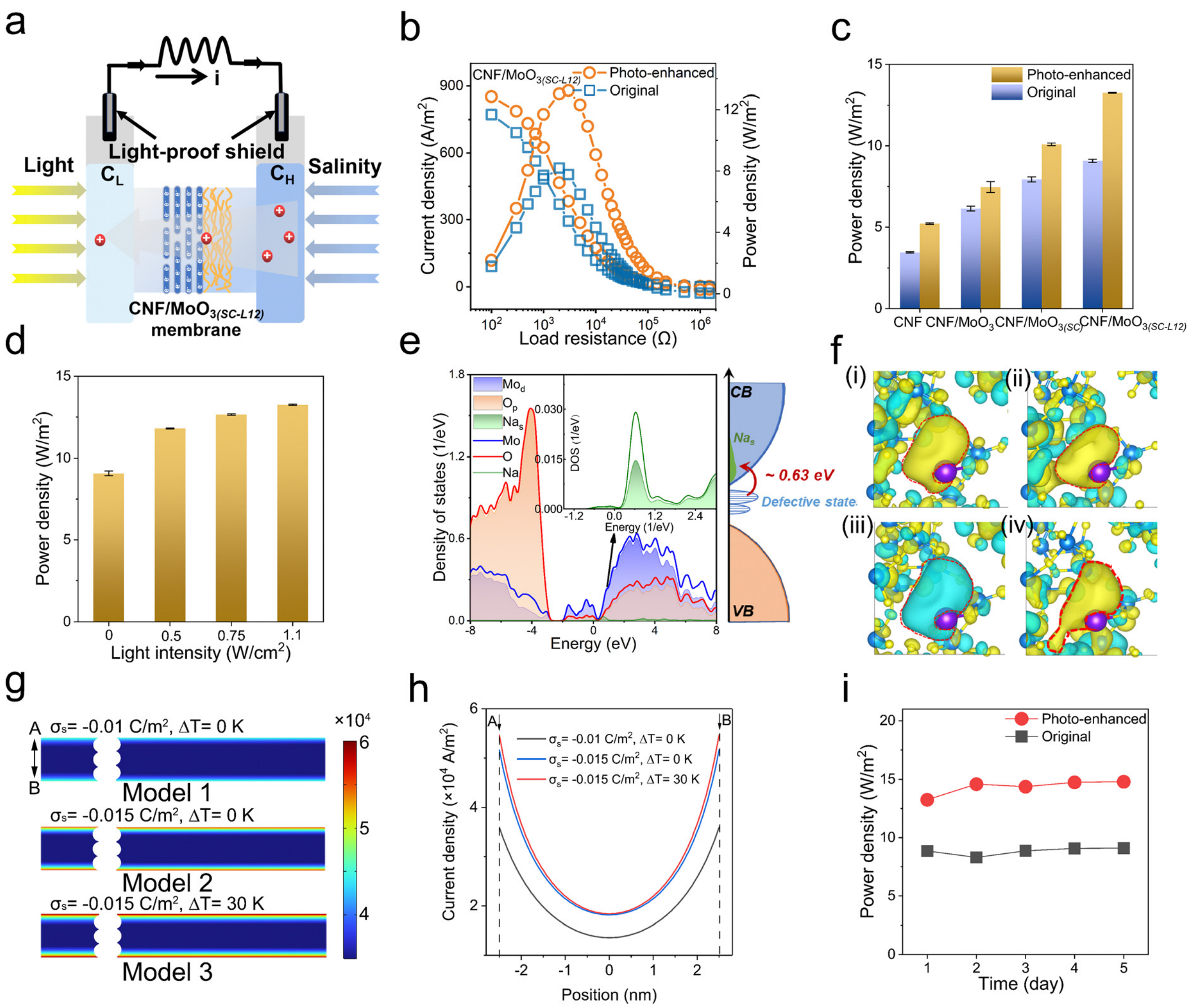

Fig. 5 Photo-enhanced osmotic energy conversion. (a) Schematic of the solar-osmotic power generation system. Light illumination (~1.1 W cm^{-2}) was on the MoO_3 side (the position close to the low concentration side) of the membrane. (b) Power generation of $CNF/MoO_{3(SC-L12)}$ with and without light irradiation. (c) Output power density of pristine CNF, CNF/MoO_3, $CNF/MoO_{3(SC)}$, and $CNF/MoO_{3(SC-L12)}$ membranes before and after light irradiation. (d) Osmotic energy conversion performance of heterogeneous $CNF/MoO_{3(SC-L12)}$ nanofluidic membranes under different light intensities. (e) DOS of the amorphous $MoO_{2.7}$ with Na^+ adsorption. Inset: DOS of Na_s. (f) Excited-state electron spatial distributions at different excitation energies (i–iii: 1.006 eV; iv: 1.993 eV; purple ball: Na^+; yellow and cyan: excited state electrons). (g) and (h) PNP simulation results of the current density distribution based on the 2D channels of the three models. (i) The working stability of the $CNF/MoO_{3(SC-L12)}$ membrane in osmotic energy conversion with and without light illumination.

employed to provide deep insights into the synergistic effect of the photo-induced temperature and surface charge increase in the nanofluidic membranes (Fig. 5g and h and Note S6, ESI†).[21,56,57] For simplicity, considering the structural characteristics of the composite nanofluidic membranes, a simplified 2D nanochannel with a length of 1000 nm, a width of 200 nm, and a height of 5 nm was used to simulate ion transport performance (Fig. S24, ESI†). To simplify the model, the surface charge and temperature are set within reasonable ranges according to the given experimental results and relevant reports (Fig. 5g). By introducing increased surface charge and thermal effects, three models with different cofactors were simulated to investigate the energy conversion performance and current density distribution (Fig. 5g and h). The current density of model 2 (σ_{surface} = 0.015 C m^{-2}, ΔT = 0 K) was higher than that of model 1 (σ_{surface} = 0.01 C m^{-2}, ΔT = 0 K), indicating that the increase of surface charge enhances ion selectivity and thus promotes energy conversion. The current density of model 3 (σ_{surface} = 0.015 C m^{-2}, ΔT = 30 K) was higher than that of model 2, indicating that the increase of ion migration caused by an additional temperature gradient could also improve the energy conversion. At the same time, model 3 had the highest current density among all models, suggesting the significant roles of temperature and charge density in accelerating ion diffusion. Therefore, the PNP simulation supported the experimental measurements and provided visual current density distributions for analysis. The cycle power density measurement showed no obvious attenuation, indicating the long-term stability and promising application potential of the system (Fig. 5i).

Conclusions

In summary, we designed an efficient solar-osmotic energy conversion system assisted by SPR and photothermal effects based on heterogeneous CNF/MoO_3 nanofluidic membranes. By mixing 0.01/0.5 M NaCl solutions, the maximum power density reached 7.86 W m^{-2}. We have shown that SPR can regulate selective cation transport and substantially boost osmotic energy conversion ($\sim$9.07 W m^{-2}). By DFT simulations, we confirmed the regulation of electronic and optoelectronic properties on the surface of MoO_3 by SPR. In combination with PNP simulations, we showed that the higher surface charge and temperature of the nanofluidic membranes tuned by SPR and photothermal effects help to improve ion selectivity and accelerate cation diffusion. Benefiting from the introduction of SPR and photothermal effects, the output power density can achieve a remarkable value of $\approx$13.24 W m^{-2}. This work introduced a novel strategy for ion transport regulation through changing the surface properties of nanofluidic membranes based on SPR. We also envision that this design not only brightens prospects in osmotic energy conversion, but also opens the exploration of advanced materials with multiple intelligent response couplings for ion gathering, desalination, and energy storage.

Experimental section

Materials

MoS_2 powder was provided by Sigma-Aldrich (Fluka, product number: 69860). Ethanol of analytical grade was purchased from Sinopharm Chemical Reagent Co., Ltd. (China). CO_2 with a purity of 99.99% was purchased from the Zhengzhou Yuanzheng Technology Development Co., Ltd. TEMPO oxidized CNF gel (1.22 wt%) was purchased from Tianjin Woodelfbio Cellulose Co., Ltd. Nylon filter film (N66, an average pore size of 50 nm) was purchased from Haining Yibo Filter Equipment Factory. All the chemicals including sodium chloride (NaCl) and potassium chloride (KCl) were analytically pure.

Preparation of amorphous MoO_3 nanosheets

The typical process is as follows: MoS_2 (100 mg) was dispersed in an aqueous solution (10 mL) with 45% ethanol volume fraction and ultrasonically treated for 4 h to form a uniform solution. It was then dried in a constant temperature oven at 60 °C. MoO_3 was prepared by annealing the pre-treated MoS_2 at 350 °C for 90 min. The resulting MoO_3 was dispersed in a 45% ethanol/water mixture (10 mL) followed by ultrasound treatment for 60 minutes to achieve good dispersion. The dispersion was then quickly transferred to a SC-CO_2 unit, which consisted primarily of a stainless-steel autoclave with a heating jacket and a temperature controller. The autoclave was heated to 80 °C and CO_2 was filled into the reactor to the required pressure (20 MPa). After a 3 h reaction, CO_2 was released slowly. The dispersion was then centrifuged at 6000 rpm for 15 min, the aggregates were removed at room temperature, and the supernatant was collected.

Preparation of heterogeneous nanofluidic membranes

The CNF solution (2 mL, 1 mg mL^{-1}) was first filtered for 45 min to form the membrane, and then the according MoO_3 solution 2 mL, 1 mg mL^{-1}, MoO_3: ultrasonicated; $MoO_{3(SC)}$: SC-CO_2 treated; $MoO_{3(SC\text{-}L12)}$: light irradiation for 12 minutes after SC-CO_2 treatment and immediately filtered for another 2 hours to form the heterogeneous nanofluidic composite membranes.

The intercalation mechanism is as follows:

$$MoO_3 \rightarrow MoO_3{}^* + h^+ + e^- \tag{4}$$

$$2h^+ + H_2O \rightarrow 2H^+ + \frac{1}{2}O_2 \tag{5}$$

$$MoO_3 + xH^+ + xe^- \rightarrow H_xMoO_3 \tag{6}$$

Density functional theory (DFT) simulations

Density functional theory (DFT) simulations were performed using the CP2K software package. The Gaussian plane wave (GPW) method, which combines the double-zeta-polarized Gaussian basis set optimized for condensed systems and the plane-wave basis set (with an energy cutoff of 400 Ry), was employed to efficiently solve the DFT Kohn–Sham equation. Additionally, the ion–electron interaction was accounted for using the GTH norm-conserving pseudopotential. All structures were thoroughly optimized using the Broyden–Fletcher–Goldfarb–Shanno (BFGS) minimization algorithm, the geometry change was converged within 3E−3 bohr, the root mean square (RMS) of the geometry change was converged within 1.5E−3 bohr, the force was converged within 4.5E−4 bohr/hartree, and the RMS of force was converged within 3E−4 bohr/hartree. The selection of the exchange–correlation functional plays a pivotal role in determining the precision of the simulation. Consequently, for tasks such as structural optimization and molecular dynamics simulations, the *meta*-GGA R2SCAN functional in conjunction with the DFT-D3 dispersion correction scheme was employed. This approach is recognized for its ability to accurately determine the structure of transition metal oxides. Furthermore, the use of hybrid functionals is essential for deriving reliable electronic structures of transition metal oxides. As such, the B3LYP functional was utilized to calculate the electronic state density and electronic excitations. In addition, the study of excited states was accelerated by the Tamm–Dancoff approximation. The excited state energy produced by this method is essentially the same as that obtained from the time-dependent density functional theory itself, when the same exchange–correlation functional is used.

In this research, a melt-quenching scheme, underpinned by molecular dynamics simulations, was used to generate amorphous structures. Specifically, the initial crystal structure was subjected to complete melting at a temperature of 2500 K, yielding a high-temperature amorphous structure. This structure was subsequently cooled to 300 K, resulting in a room-temperature amorphous structure following comprehensive equilibrium. Throughout the series of molecular dynamics simulations, the canonical sampling through velocity-rescaling (CSVR) thermostat was employed to establish the canonical ensemble, operating at a time step of 1 fs. The radial distribution function (RDF) showed that the atomic arrangement of the final structure has typical short-range ordered and long-range disordered amorphous characteristics.

Numerical simulations

The thermoelectric conversion phenomenon was theoretically investigated using the commercial finite-element software package COMSOL Multiphysics (version 5.4; COMSOL Inc., Stockholm, Sweden) based on "electrostatics (Poisson equation)" and "Nernst–Planck without Electroneutrality" modules. The coupled governing Poisson–Nernst–Planck (PNP) equations are shown below.

$$J_\mathrm{i} = D_\mathrm{i}\left(\nabla c_\mathrm{i} + \frac{z_\mathrm{i} F c_\mathrm{i}}{\mathrm{RT}}\nabla\varphi\right) + c_\mathrm{i} u \tag{7}$$

$$\nabla^2\varphi = -\frac{F}{\varepsilon}\sum z_\mathrm{i} c_\mathrm{i} \tag{8}$$

$$\nabla \cdot J_\mathrm{i} = 0 \tag{9}$$

Here, the physical quantities J_i, D_i, c_i, φ, u, R, F, T, and ε refer to the ionic flux, diffusion coefficient, ion concentration, electrical potential, fluid velocity, universal gas constant, Faraday constant, absolute temperature, and dielectric constant of the electrolyte solutions, respectively. Eqn (7) shows the Nernst–Planck equation which describes the transport properties of a charged nanochannel. Eqn (8) shows the Poisson equation which describes the relationship between the electrical potential and ion concentrations. Besides, the flux should satisfy the time-independent continuity equation (eqn (9)) when the system reaches a stationary regime. A simplified negatively charged (σ = −0.01 C m^{-2} and −0.015 C m^{-2}) channel with a length of 1000 nm, a width of 200 nm, and a height of 5 nm was chosen as the simulated model. To carry out the calculations, the "electrostatics (AC/DC)" and "Nernst–Plank without electroneutrality" modules were used. In addition, to precisely set the temperature of the channel, the "heat transfer in fluids" module was coupled to this model. The model with a temperature difference of 30 K (room temperature is set to 298 K) was applied. The coupled equations (eqn (7)–(9)) must be solved for a given geometry using appropriate boundary conditions.

The boundary condition for the potential φ on the channel wall is

$$\underset{n}{\rightarrow} \cdot \nabla\varphi = -\frac{\sigma}{\varepsilon} \tag{10}$$

The ion flux has zero normal components at the boundaries:

$$\underset{n}{\rightarrow} \cdot J = 0 \tag{11}$$

The parameter σ (σ is set to −0.01 C m^{-2} and −0.015 C m^{-2}) is the surface charge density of the channel walls. Then, the ionic current can be calculated by

$$I = \int \mathrm{sF}\left(Z_\mathrm{p} j_\mathrm{p} + Z_\mathrm{n} j_\mathrm{n}\right) \cdot \underset{n}{\rightarrow} \mathrm{d}s \tag{12}$$

Conflicts of interest

There are no conflicts to declare.

Acknowledgements

This work was financially supported by the National Natural Science Foundation of China (Grant no. 22305228 and 21773216), the Postdoctoral Fellowship Program of CPSF (Grant no. GZC20232380), and the joint project from the Henan-Provincial and the China-National Natural Science Foundation (Project No. U2004208).

References

1 D. Griggs, M. Stafford-Smith, O. Gaffney, J. Rockström, M. C. Ö. Hman, P. Shyamsundar, W. Steffen, G. Glaser, N. Kanie and I. Noble, *Nature*, 2013, **495**, 305–307.

2 B. Obama, *Science*, 2017, **355**, 126–129.

3 C. F. Shih, T. Zhang, J. Li and C. Bai, *Joule*, 2018, **2**, 1925–1949.

4 H. Wu, H. L. Tan, C. Y. Toe, J. Scott, L. Wang, R. Amal and Y. H. Ng, *Adv. Mater.*, 2020, **32**, e1904717.

5 A. Siria, M.-L. Bocquet and L. Bocquet, *Nat. Rev. Chem.*, 2017, **1**, 0091.

6 B. E. Logan and M. Elimelech, *Nature*, 2012, **488**, 313–319.

7 X. Tong, S. Liu, J. Crittenden and Y. Chen, *ACS Nano*, 2021, **15**, 5838–5860.

8 Z. Zhang, L. Wen and L. Jiang, *Nat. Rev. Mater.*, 2021, **6**, 622–639.

9 L. Yang and L. Wen, *Cell Rep. Phys. Sci.*, 2022, **3**, 101167.

10 W. Xin, L. Jiang and L. Wen, *Acc. Chem. Res.*, 2021, **54**, 4154–4165.

11 T. Huang, X. Kan, J. Fan, H. Gao, L. Yu, L. Zhang, J. Xia, J. Gao, X. Liu, K. Sui and L. Jiang, *ACS Nano*, 2023, **17**, 17245–17253.

12 P. Liu, X.-Y. Gao, L.-J. Zhang, W. Chen, Y. Hu, X.-Y. Kong, X.-B. Li, L. Wen, C.-H. Tung, L.-Z. Wu and L. Jiang, *CCS Chem.*, 2023, **5**, 2012–2022.

13 Q. Wang, Y. Wu, C. Zhu, Y. Hu, L. Fu, Y. Qian, T. Li, X. Li, Z. Zhang, X. Y. Kong, L. Jiang, Z. Zhang and L. Wen, *Angew. Chem., Int. Ed.*, 2023, **62**, e202302938.

14 K. Xiao and O. G. Schmidt, *CCS Chem*, 2021, **3**, 2938–2949.

15 P. Liu, L. Jiang and L. Wen, *Nano Res.*, 2023, **16**, 10061–10071.

16 Y. Zhou, T. Xiong, J. Lu, P. Yu, Y. Jiang, F. Xia and L. Mao, *Angew. Chem., Int. Ed.*, 2023, **62**, e202302997.

17 K. Xiao, L. Chen, R. Chen, T. Heil, S. D. C. Lemus, F. Fan, L. Wen, L. Jiang and M. Antonietti, *Nat. Commun.*, 2019, **10**, 74.

18 J. Yang, X. Hu, X. Kong, P. Jia, D. Ji, D. Quan, L. Wang, Q. Wen, D. Lu, J. Wu, L. Jiang and W. Guo, *Nat. Commun.*, 2019, **10**, 1171–1177.

19 K. Xiao, P. Giusto, F. Chen, R. Chen, T. Heil, S. Cao, L. Chen, F. Fan and L. Jiang, *Natl. Sci. Rev.*, 2021, **8**, nwaa231.

20 P. Liu, T. Zhou, Y. Teng, L. Fu, Y. Hu, X. Lin, X.-Y. Kong, L. Jiang and L. Wen, *CCS Chem.*, 2020, **2**, 1325–1335.

21 P. Liu, T. Zhou, L. Yang, C. Zhu, Y. Teng, X.-Y. Kong and L. Wen, *Energy Environ. Sci.*, 2021, **14**, 4400–4409.

22 S. Zhou, Z. Qiu, M. Strømme and C. Xu, *Energy Environ. Sci.*, 2021, **14**, 900–905.

23 B. Verberck, *Nat. Phys.*, 2017, **13**, 205.

24 T. Ge, Z. Wei, X. Zheng, P. Yan and Q. Xu, *J. Phys. Chem. Lett.*, 2021, **12**, 6543–6550.

25 Y. Ren and Q. Xu, *Energy Environ. Mater.*, 2018, **1**, 46–60.

26 L. Du, B. Gao, S. Xu and Q. Xu, *Nat. Commun.*, 2023, **14**, 2278.

27 T. Ge, W. Cui and Q. Xu, *Angew. Chem., Int. Ed.*, 2023, **62**, e202300446.

28 W. Liu, Q. Xu, W. Cui, C. Zhu and Y. Qi, *Angew. Chem., Int. Ed.*, 2017, **56**, 1600–1604.

29 M. M. Alsaif, K. Latham, M. R. Field, D. D. Yao, N. V. Medhekar, G. A. Beane, R. B. Kaner, S. P. Russo, J. Z. Ou and K. Kalantar-zadeh, *Adv. Mater.*, 2014, **26**, 3931–3937.

30 M. M. Y. A. Alsaif, A. F. Chrimes, T. Daeneke, S. Balendhran, D. O. Bellisario, Y. Son, M. R. Field, W. Zhang, H. Nili, E. P. Nguyen, K. Latham, J. van Embden, M. S. Strano, J. Z. Ou and K. Kalantar-zadeh, *Adv. Funct. Mater.*, 2016, **26**, 91–100.

31 I. A. de Castro, R. S. Datta, J. Z. Ou, A. Castellanos-Gomez, S. Sriram, T. Daeneke and K. Kalantar-zadeh, *Adv. Mater.*, 2017, **29**, 1701619.

32 V. Kumar, A. Sumboja, J. Wang, V. Bhavanasi, V. C. Nguyen and P. S. Lee, *Chem. Mater.*, 2014, **26**, 5533–5539.

33 J. Kalikka, X. Zhou, E. Dilcher, S. Wall, J. Li and R. E. Simpson, *Nat. Commun.*, 2016, **7**, 11983.

34 Y. Qi, Q. Xu, Y. Wang, B. Yan, Y. Ren and Z. Chen, *ACS Nano*, 2016, **10**, 2903–2909.

35 K. F. Mak, C. Lee, J. Hone, J. Shan and T. F. Heinz, *Phys. Rev. Lett.*, 2010, **105**, 136805.

36 L. Zheng, Y. Xu, D. Jin and Y. Xie, *Chem. Mater.*, 2009, **21**, 5681–5690.

37 R. B. Schoch, J. Han and P. Renaud, *Rev. Mod. Phys.*, 2008, **80**, 839–883.

38 A. Siria, P. Poncharal, A. L. Biance, R. Fulcrand, X. Blase, S. T. Purcell and L. Bocquet, *Nature*, 2013, **494**, 455–458.

39 J. Feng, M. Graf, K. Liu, D. Ovchinnikov, D. Dumcenco, M. Heiranian, V. Nandigana, N. R. Aluru, A. Kis and A. Radenovic, *Nature*, 2016, **536**, 197–200.

40 R. B. Schocha and P. Renaud, *Appl. Phys. Lett.*, 2005, **86**, 253111.

41 D. Stein, M. Kruithof and C. Dekker, *Phys. Rev. Lett.*, 2004, **93**, 035901.

42 S. Hirata and M. Head-Gordon, *Chem. Phys. Lett.*, 1999, **314**, 291–299.

43 N. Liao, B. Zheng, M. Zhang and W. Xue, *J. Mater. Chem. A*, 2016, **4**, 12328–12333.

44 D. Mora-Fonz and A. L. Shluger, *Phys. Rev. B*, 2019, **99**, 014202.

45 Y. Cheng, Q. Yang, J. Wang, T. Dimitriadis, M. Schumacher, H. Zhang, M. J. Müller, N. Amini, F. Yang, A. Schoekel, J. Pries, R. Mazzarello, M. Wuttig, H.-B. Yu and S. Wei, *Nat. Commun.*, 2022, **13**, 7352.

46 G. Drewelow, A. Reed, C. Stone, K. Roh, Z.-T. Jiang, L. N. T. Truc, K. No, H. Park and S. Lee, *Appl. Surf. Sci.*, 2019, **484**, 990–998.

47 S. Fan, S. J. Yun, W. J. Yu and Y. H. Lee, *Adv. Sci.*, 2020, **7**, 1902751.

48 S. H. Cho, J. Byeon, K. Jeong, J. Hwang, H. Lee, J. Jang, J. Lee, T. Kim, K. Kim, M. Choi and Y. S. Lee, *Adv. Energy Mater.*, 2021, **11**, 2100555.

49 J. A. Scholl, A. L. Koh and J. A. Dionne, *Nature*, 2012, **483**, 421–427.

50 H. Chen, L. Shao, Q. Li and J. Wang, *Chem. Soc. Rev.*, 2013, **42**, 2679–2724.

51 X. Lin, P. Liu, W. Xin, Y. Teng, J. Chen, Y. Wu, Y. Zhao, X. Y. Kong, L. Jiang and L. Wen, *Adv. Funct. Mater.*, 2021, **31**, 2105013.

52 D.-K. Kim, C. Duan, Y.-F. Chen and A. Majumdar, *Microfluid. Nanofluid.*, 2010, **9**, 1215–1224.

53 X. Liu, M. He, D. Calvani, H. Qi, K. Gupta, H. J. M. de Groot, G. J. A. Sevink, F. Buda, U. Kaiser and G. F. Schneider, *Nat. Nanotechnol.*, 2020, **15**, 307–312.

54 C. Zhu, X. Zuo, W. Xian, Q. Guo, Q.-W. Meng, S. Wang, S. Ma and Q. Sun, *ACS Energy Lett.*, 2022, **7**, 2937–2943.

55 X. Zuo, C. Zhu, W. Xian, Q. W. Meng, Q. Guo, X. Zhu, S. Wang, Y. Wang, S. Ma and Q. Sun, *Angew. Chem., Int. Ed.*, 2022, **61**, e202116910.

56 H. S. White and A. Bund, *Langmuir*, 2008, **24**, 12062–12067.

57 G. Xie, P. Li, Z. Zhang, K. Xiao, X.-Y. Kong, L. Wen and L. Jiang, *Adv. Energy Mater.*, 2018, **8**, 1800459.